CHEMISTRY OF MATERIALS

pubs.acs.org/cm

Article

$Zn_3GaB_6O_{12}As$ and $Zn_4P_6N_{12}S$: Isotropic Zero Thermal Expansion Materials Based on the "Cage-Restricting" Model

Youquan Liu, Xingxing Jiang,* Maxim S. Molokeev, Xingyu Zhang, and Zheshuai Lin*

Cite This: *Chem. Mater.* 2022, 34, 9915−9922

Read Online

ACCESS | Metrics & More | Article Recommendations | Supporting Information

ABSTRACT: With the capability to keep the size invariant along all dimensions over a certain temperature range, isotropic zero thermal expansion (ZTE) materials have been attracting wide interest in many scientific and engineering fields. Herein, based on the "cage-restricting" model for the ZTE materials with β-sodalite-like structures, we design and synthesize two new isotropic ZTE materials, $Zn_3GaB_6O_{12}As$ (ZGBA) and $Zn_4P_6N_{12}S$ (ZPNS), from the molecular engineering strategies of enhancing the cage-restricting force and of increasing the rigidity of β-sodalite cages, respectively. ZGBA and ZPNS exhibit isotropic ZTE behaviors in the temperature range from 20 to 300 K, with the coefficients of thermal expansion 1.18(17)/MK and 1.37(17)/MK, respectively, both of which are lowered by ∼30−20% in comparison with their template compound $Zn_4B_6O_{12}S$ (ZBS). The mechanisms of improved isotropic ZTE in ZGBA and ZPNS are unraveled by lattice dynamic analysis and temperature-dependent crystal structure evolution. This study paves new avenues to enhance the ZTE behavior in the materials with cage-like structures and has great implication on the exploration of isotropic ZTE materials.

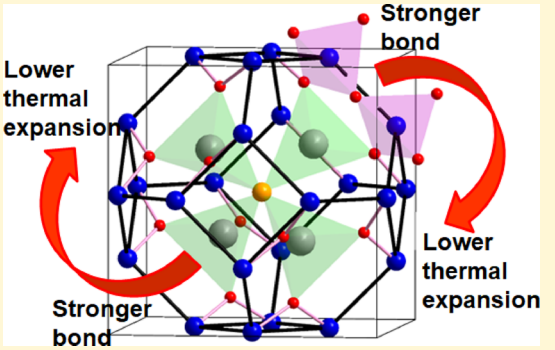

INTRODUCTION

The "heat expansion and cold contraction" response in conventional materials is known to deteriorate the performance stability and accuracy of precise apparatuses that are operated in temperature-fluctuating environments. By virtue of the temperature-independent size, zero thermal expansion (ZTE) materials (with the linear coefficient of thermal expansion, CTE, in the range ∼±2.0 MK^{-1} and strictly ∼±1.0 MK^{-1})[1] can provide an effective solution to this problem, thus holding great promise in many applications, for example, electronic devices,[2] advanced optical apparatuses,[3] and precision structural engineered parts,[4−8] where a high thermal shock resistance is required on the adopted materials. In particular, the isotropic ZTE materials can perfectly eliminate the inhomogeneity of thermal stress and are considered to be more suitable for practical applications.[9] From the aspect of rational material design, however, it is a big challenging task to achieve the subtle expansion−contraction balance among the temperature-dependent structural variation of constituent microscopic units in isotropic crystal lattices to make the thermal expansion of macroscopic size negligible; till now, isotropic ZTE behaviors have only been detected in a dozen or so materials.[9−21]

Suppression of the rotation of (quasi-)rigid polyhedra in a cubic lattice framework is a dominant structure-regulating method to realize the isotropic ZTE behavior.[13,14,20,22−24] Accordingly, a handful of isotropic ZTE materials have been discovered in the past decades, such as $Fe[Co(CN)_6]$,[20] $MgZrF_6$,[11] TaO_2F,[13] $YbZrF_7$,[15] $N(CH_3)_4CuZn(CN)_4$,[17] and $Zr_{0.4}Sn_{0.6}Mo_2O_8$.[14] All these materials are exclusively constructed by open frameworks with large cavities. Since 2016, our group has studied the isotropic ZTE property in densified framework materials and discovered isotropic near-ZTE behaviors with the CTEs of ∼1.5 MK^{-1} (from 5 to 300 K) in the $Zn_4B_6O_{12}X$ (ZBX) family[12,25] (X = O, S, or Se, abbreviated as ZBO, ZBS, or ZBSe, respectively). The three compounds in the ZBX family are isostructural, and their structures are shown in Figure 1a (taking ZBS as the representative). ZBX is crystallized in the cubic *I-43m* space group, with 24 $[BO_4]$ tetrahedra connected to one another by sharing the cornered O atoms to form a closed β-sodalite $[B_{24}O_{48}]$ cage in a unit cell. Remarkably, four Zn^{2+} cations are trapped in each cage and coordinated with the surrounding atoms to form four $[ZnO_3X]$ tetrahedral groups; each Zn^{2+} cation is bonded to three O^{2-} anions (two-coordinate) on the cage and to the X^{2-} anion (four-coordinate) at the cage center. While the anions of O^{2-}, S^{2-}, and Se^{2-} at the X sites have little influence on the thermal expansion,[12,25] the restriction of Zn−

Received: June 29, 2022
Revised: October 25, 2022
Published: November 4, 2022

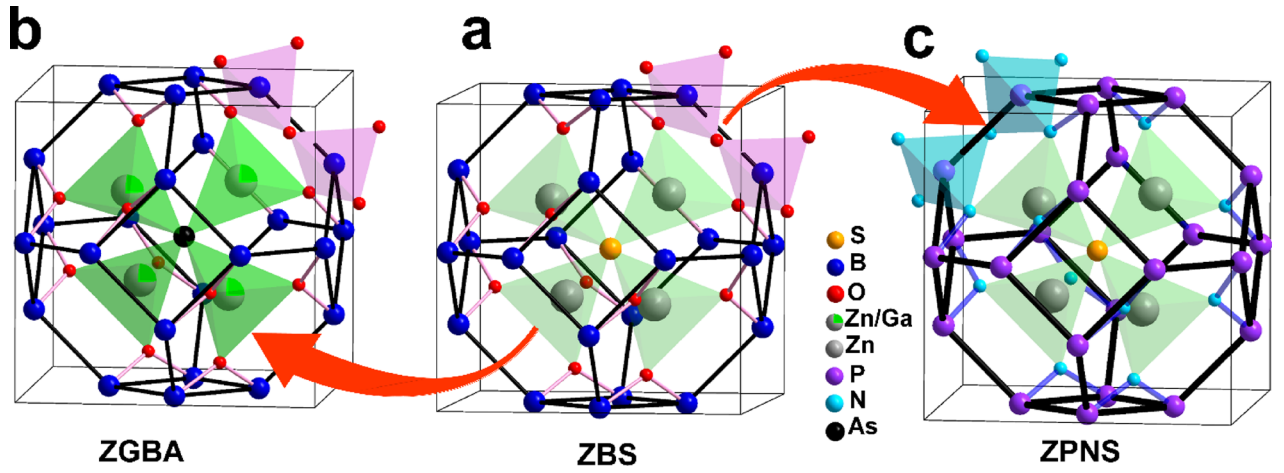

Figure 1. Structure evolution from ZBS (a) to ZGBA (b) and to ZPNS (c). The $[ZnO_3S]$ tetrahedra in ZBS are replaced with the $[Zn_{0.75}/Ga_{0.25}O_3As]$ tetrahedra in ZGBA, while the $[B_{24}O_{48}]$ sodalite cages formed by $[BO_4]$ groups in ZBS are replaced with the $[P_{24}N_{48}]$ cages formed by $[PN_4]$ groups in ZPNS. The magenta and blue polyhedra represent $[BO_4]$ and $[PN_4]$ groups, respectively. The Zn-centered and $Zn_{0.75}/Ga_{0.25}$-centered tetrahedra are marked by light green and dark green colors, respectively.

O bonds in the $[ZnO_3X]$ groups suppresses the rotation of $[BO_4]$ tetrahedral groups within the cage, which significantly lowers the thermal expansion of the cage and leads to the isotropic ZTE in the macroscopic size of these three compounds. This mechanism has been elaborated by the "cage-restricting" model.[12,25]

According to the "cage-restricting" model, two effective strategies would be expected to further suppress the polyhedral rotation to enhance the isotropic ZTE effect in the β-sodalite-like materials: (i) strengthening the binding force to the sodalite cage by adopting atoms with higher electronegativity to replace the zinc atoms and (ii) increasing the rigidity of the sodalite cage itself by using the units with higher covalence to replace the $[BO_4]$ tetrahedra. In this work, following these two molecular design strategies, we successfully synthesize two compounds, $Zn_3GaB_6O_{12}As$ (ZGBA) and $Zn_4P_6N_{12}S$ (ZPNS), respectively. Both compounds manifest the enhanced isotropic ZTE effects, with the CTEs lowered by ~30−20% compared to that of the ZBX family, from 20 to 300 K. The ZTE mechanisms in ZGBA and ZPNS are elaborated by the lattice dynamical analysis from Raman measurements combined with the structural evolution from the first-principles simulations, which verifies the validity of our adopted ZTE design strategies.

EXPERIMENTAL AND COMPUTATIONAL METHODS

Synthesis. ZGBA was synthesized by ZnO (Sinopharm Chemical Reagent Co., Ltd., 99.7%), GaAs (Macklin Biochemical Chemical Co., Ltd., 99.0%), and B_2O_3 (Sinopharm Chemical Reagent Co., Ltd., 99.7%) mixed in the ratio of 3:1:3 and fully grounded under argon atmosphere in a glovebox. The ground mixture was placed in a quartz tube and sealed in a vacuum of 10^{-5} Pa. Then, the sealed glass quartz tube was placed in a muffle furnace, slowly heated up to 400 °C at the heating rate of 0.2 °C/min, and maintained at this temperature for 1440 min. After cooling to room temperature, the sample was re-grinded in the glovebox. Then, the sample was sealed again in a quartz tube, heated up to 900 °C at 0.2 °C/min, and kept for 7200 min. After cooling to room temperature, a white target compound in powder form was obtained.

ZPNS has been synthesized according to equation (1). $ZnSO_4$ (Sinopharm Chemical Reagent Co., Ltd., 99.7%), P_3N_5 (Macklin Biochemical Chemical Co., Ltd., 99.0%), and Zn_3N_2 (Aladdin Chemical Reagent Co., Ltd., 99.0%) were weighed according to the stoichiometric ratio in eq (1) and fully ground using an agate mortar under argon atmosphere in a glovebox. The mixture was placed into a quartz tube and sealed in a vacuum of 10^{-5} Pa, then heated up to 830 °C at 0.2 °C/min in a muffle furnace, and maintained at this temperature for 7 days. Subsequently, a white compound in powder form was obtained, with the quartz tube naturally cooling to room temperature.

$$ZnSO_4 + Zn_3N_2 + 2P_3N_5 \xrightarrow{830^{\circ}C} Zn_4P_6N_{12}S + 2O_2\uparrow \quad (1)$$

Variable-Temperature XRD Measurements from 20 to 300 K. The VT-XRD data were measured on ZGBA for 6 h and on ZPNS for 6 h (first) and 14 (second) h by using a Rigaku Smartlab instrument. The crystal structure at 300 K was refined by the Rietveld method with TOPAS[26] using the structure of $Zn_4B_6O_{12}S$ as a template,[25] in which S was replaced by As and Zn was replaced by fractionally occupied $Zn_{0.75}Ga_{0.25}$, respectively. Then, based on the structure at 300 K, the cell parameters at the respective temperatures were further refined. The attempted structure in which Ga^{3+} is placed at the borate site or As^{3-} is located at the oxygen site failed, confirming the uniqueness of the solved structure.

Variable-Temperature Raman Spectra Measurements from 93 to 293 K. The variable-temperature Raman spectra (VT-RS) were measured by using a LabRAM HR Evolution Raman apparatus with 532 nm laser.

Energy-Dispersive Spectroscopy and Elemental Analysis. SEM and energy-dispersive X-ray spectroscopy (EDS) for the elemental analysis of ZGBA were performed using a Hitachi S4300 field emission scanning electron microscope and a Nikon inverted optical microscope (Eclipse Ti-U) with a CCD. The lowest imaging voltage of this device is 10 eV, which is difficult to detect for the light element B.[27] We mainly investigate the element distribution and proportion of Zn, Ga, As, and O atoms (Figures S1−S3). The elements of Ga, Zn, As, and O are evenly distributed on the sample, which indicated the phase homogeneity of the bulk sample. Finally, the element ratio according to the EDS data is 1.03 (Ga):3.24 (Zn):1.00 (As):17.26 (O) (Table S1). Combined with XRD and infrared spectra, it can be determined that the synthesized sample is ZGBA.

Thermal Expansion Coefficient. The ZTE behavior of ZGBA and ZPNS was tested by the PASCal program.[28] The thermal expansion coefficients are obtained from the Rietveld method, the results of which were refined different temperatures. In order to investigate the ZTE mechanism of ZGBA in detail, only the lattice parameters of ZGBA in the test sample are considered to avoid the influence of $ZnGa_2O_4$ and GaAs. The lattice parameters (8.2067 Å) of

https://doi.org/10.1021/acs.chemmater.2c01947
Chem. Mater. 2022, 34, 9915−9922

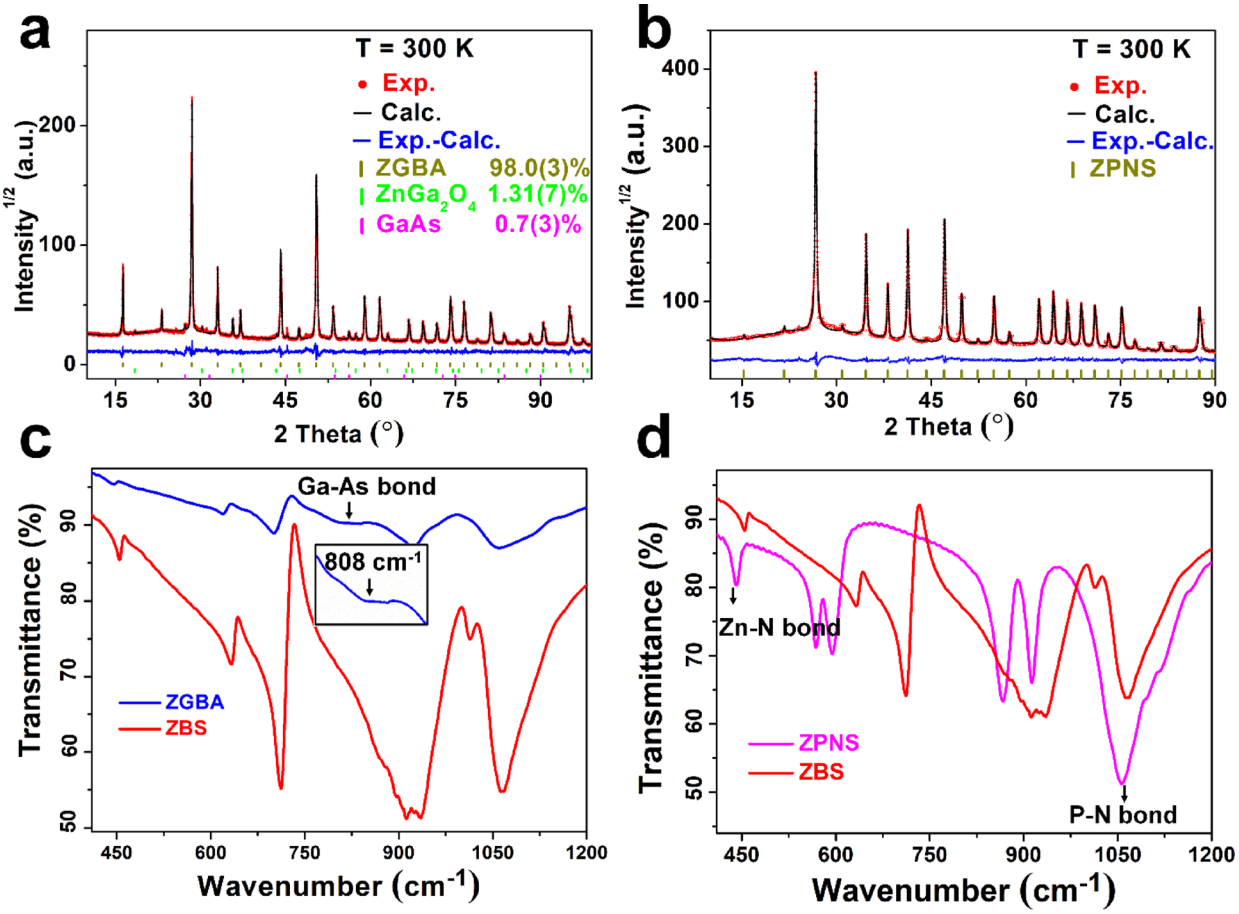

Figure 2. Rietveld refinement plots of the X-ray diffraction (XRD) data (@300 K) in ZGBA (a) and ZPNS (b). Because a small amount of GaAs was oxidized during the synthesis process of ZGBA, trace $ZnGa_2O_4$ is presented in the XRD pattern. Infrared spectra of ZGBA (c) and ZPNS (d), with the ZBS spectra shown for comparison. The characteristic absorption peak for Ga−As bonds (@808 cm^{-1}) is enlarged in the inset in (c).

ZPNS at 180 K are significantly larger than those at 160 K (8.2044 Å) and 200 K (8.2049 Å), which have an obvious influence on the calculation of CTEs by PASCal. Therefore, we calculated the CTEs, concluding the lattice parameters of 180 K (1.11 MK^{-1}(0.46)) and the lattice average parameters of 180 K (0.58 MK^{-1}(0.14)), respectively. According to the first and second results of ZPNS, the CTEs from 20 to 200 K with the lattice average parameters (8.20465 Å) of 180 K are more reasonable.

Infrared Spectroscopy. The infrared sample is a mixture of ZGBA (or ZPNS) with KBr, and the weight ratio is about 1:100. Before the test, it was treated at 200°C for 5 min to remove the adsorbed water. Then, it is pressed into a transparent wafer by hydraulic press. The IR spectrum was obtained in the range of 400−2000 cm^{-1}.

First-Principles Simulations. The first-principles calculations were performed by plane-wave pseudopotential density functional theory implemented by the CASTEP package.[29,30] The exchange−correlation energy was described by the PBE[31] (Perdew, Burke, and Ernzerhof) functionals in the form of generalized gradient approximation (GGA).[32] The optimized norm-conserving pseudopotentials were chosen to describe the effective interaction between the atom cores and valence electrons.[33] The kinetic energy cutoff was set to 600.0 eV, and a 2 × 2 × 2 Monkhorst−Pack *k*-point grid was adopted.[34] To theoretically refine the temperature evolution of bond lengths and angles in ZGBA and ZPNS, the structural optimization was performed using the Broyden−Fletcher−Goldfarb−Shanno[35] (BFGS) algorithm, with only the atomic positions relaxed and the cell parameters fixed in the experimental values at the respective temperatures. The convergence tolerance of energy, maximum force, maximum stress, and maximum displacement were set to 5.0 × 10^{-7} eV/atom, 0.001 eV/Å, 0.002 GPa, and 5.0 × 10^{-5} Å, respectively. Considering the computational accuracy and efficiency of the mixed occupation of Zn and Ga atoms in ZGBA, two of the $Zn_{0.75}Ga_{0.25}$ sites in a unit cell were defined as pure Ga atoms, and the other six were identified as pure Zn atoms. Therefore, the four kinds of possible Ga sites in ZGBA with the *P*1 space group were considered, and their Raman spectra were calculated. As pictured in Figure S7, those Raman peaks were very similar, just having some Raman peaks split at low wavenumbers (0−200 cm^{-1}). The whole calculated peaks are blue-shifted by 40 and 55 cm^{-1} in ZGBA and ZPNS, respectively, to achieve better agreement with the experiments because the GGA functional overestimates effective atomic interactions. These are referred to as lateral vibrations of the Zn/Ga atoms, with a very limited effect on the rotation of the $[BO_4]$ tetrahedron. Linear response method was adopted to simulate the lattice vibrations, where the phonon frequency is derived from the second derivative of the total energy with respect to a given perturbation.[36] The electron density map of ZBS also uses the same calculation parameters as above, and the structure file is obtained from ref 25.

RESULTS AND DISCUSSION

The polycrystalline powders of ZGBA and ZPNS were synthesized by the high-temperature solid-state reaction under vacuum environments. The indexing and refinements on the powder X-ray diffraction (PXRD) patterns (Figure 2a,b) reveal that both compounds share the same cubic space group of *I*-43*m* with ZBX. As shown in Figure 1b, the boron atoms in ZGBA, similar to those in ZBX, are four-coordinated with oxygen atoms to form the $[B_{24}O_{48}]$ sodalite cages, but the

https://doi.org/10.1021/acs.chemmater.2c01947
Chem. Mater. 2022, 34, 9915−9922

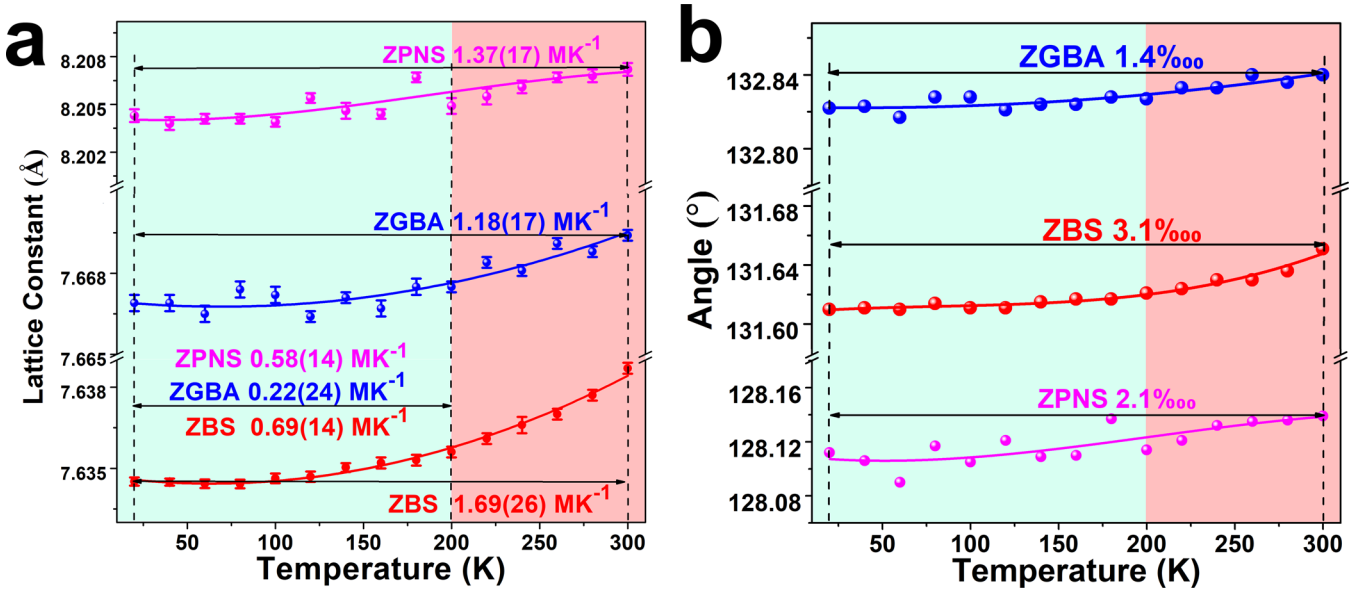

Figure 3. Variations of the refined lattice constants and CTEs (a) and the calculated variations of the ∠B−O−B or ∠P−N−P angles between the tetrahedra on sodalite cages (b) with respect to temperatures from 20 to 300 K in ZBS,[21] ZGBA, and ZPNS. The strict ZTE temperature ranges in ZBS (<200 K) are marked by green color.

Zn sites are disorderly occupied by the Zn^{2+}/Ga^{3+} cations mixed in the ratio of 3:1. Meanwhile, the cage-central X sites are occupied by As^{3-} anions to compensate the charge imbalance resulted by Zn^{2+}/Ga^{3+} doping. Thus, the Zn^{2+}/Ga^{3+} cations in ZGBA are coordinated with the neighboring As^{3-} anions to form the $[(Zn_{0.75}/Ga_{0.25})O_3As]$ tetrahedra. The $[B_{24}O_{48}]$ cages in ZGBA are restricted by Zn−O bonds (with 75% probability) and Ga−O bonds (with 25% probability) via the formed $[(Zn_{0.75}/Ga_{0.25})O_3As]$ tetrahedra. As a comparison, in ZBX, the $[B_{24}O_{48}]$ cages are restricted by Zn−O bonds solely via the $[ZnO_3X]$ tetrahedra. The Zn^{2+}/Ga^{3+} doping and As^{3-} (X-sites) occupation in ZBGA are confirmed by the presence of characteristic absorption peaks of Ga−As bonds[37] in the infrared transmission spectrum (Figure 2c) and by the uniform distribution of Ga and As in the sample (shown in Figures S1−S3 and Table S1). As the electronegativity of gallium (1.81) is higher than that of zinc (1.65), the Ga−O bonds are anticipated to be stronger than the Zn−O bonds. In ZPNS, the sodalite cages are formed by the $[PN_4]$ tetrahedra rather than by $[BO_4]$ in ZBX, whereas the ions located inside the sodalite cages (i.e., the cage-centered S^{2-} anions and Zn^{2+} cations) are the same as those in ZBS (see Figure 1c). The presence of $[PN_4]$ groups in ZPNS is confirmed by the characteristic absorption peaks of Zn−N and P−N bonds in the infrared transmission spectrum (Figure 2d). Because the P−N bonds have a higher bond valence (1.25) than that of B−O bonds (0.75), the constructed $[P_{24}N_{48}]$ cages in ZPNS are expected to be more rigid than the $[B_{24}O_{48}]$ cages in ZBX.

The VT XRD show that no new peaks emerge or old peaks vanish in both ZGBA and ZPNS from 20 to 300 K (Figures S4 and S5), confirming the absence of phase transition and thermal stability over the measured temperature range. The refined cell parameters reveal that, as temperature increases from 20 to 300 K, the lattice constants in ZGBA and ZPNS increase by just 0.033% (from 7.6669(3) to 7.6694(2) Å) and 0.035% (from 8.2043(4) to 8.2072(4) Å), respectively, manifesting the isotropic near-ZTE behaviors, with the fitted linear CTEs of 1.18(17) and 1.37(17)/MK, respectively (Figure 3a). These CTE values are lowered by 30−20% than those in the ZBX family (e.g., 1.69(0.26) MK^{-1} for ZBS; see also Figure 3a). The ZTE behaviors in ZGBA and ZPNS are comparable to those in the ever-reported isotropic ZTE materials, including $Fe[Co(CN)_6]$ (−1.47 MK^{-1}, 4.2−300 K),[20] $MgZrF_6$ (−0.79 MK^{-1}, 300−675 K),[11] TaO_2F (0.6 MK^{-1}, 200−773 K),[13] $Mn_3Cu_{0.5}Ge_{0.5}N$ (0.118 MK^{-1}, 12−230 K),[19] $TbCo_{1.9}Fe0.1$ (0.48 MK^{-1}, 123−307 K),[6] $0.8PbTiO_3$−$0.2Bi(Ni_{1/2}Ti_{1/2})O_3$ (0.38 MK^{-1}, 298−798 K),[38] and nano-sized ScF_3 (0.04 MK^{-1}, 325−675 K).[1]

In order to investigate the improved ZTE mechanism in ZGBA and ZPNS, VT-RS from 93 to 293 K were adopted to measure the thermal excitation of lattice vibrations.[39,40] Meanwhile, the first-principles phonon calculations were performed to assign the Raman-active phonon modes to real-space atomic vibrations. The good agreement between the calculated and experimental Raman spectra (e.g., @293 K; see Figure 4a,b as well as Figure S8) ensures the reasonability of these phonon assignments. Clearly, 13 main peaks are presented in the VTRS of ZGBA, defined as modes 1−13, following the successive wavenumber order, and 8 main peaks are presented in the spectra of ZPNS, defined as modes i−viii successively. The phonon assignments reveal that these Raman peaks can be sorted into four types of atomic vibrations (Figure 4c,d): (i) Type I: the stretching vibrations of $Zn_{0.75}/Ga_{0.25}$−O bonds in ZGBA and of Zn−N bonds in ZPNS (modes 1 and 2 in ZGBA, and modes i and ii in ZPNS); (ii) Type II: the transversal vibrations of cage-centered As atoms in ZGBA and of S atoms in ZPNS (mode 3 in ZGBA and mode iii in ZPNS); (iii) Type III: the rotation vibrations of $[BO_4]$ in ZGBA and $[PN_4]$ in ZPNS (modes 4−11 in ZGBA and modes iv−vi in ZPNS); and (iv) Type IV: the stretching vibrations of B−O bonds and of P−N bonds on the sodalite cages (modes 12 and 13 in ZGBA and modes vii and viii in ZPNS).

The "cage-restricting" model shows that the thermal expansions below room temperature in the previously known ZTE materials (ZBO, ZBS, and ZBSe) in the β-sodalite family are dominantly driven by the Type III vibrations,[25] that is, the

https://doi.org/10.1021/acs.chemmater.2c01947
Chem. Mater. 2022, 34, 9915−9922

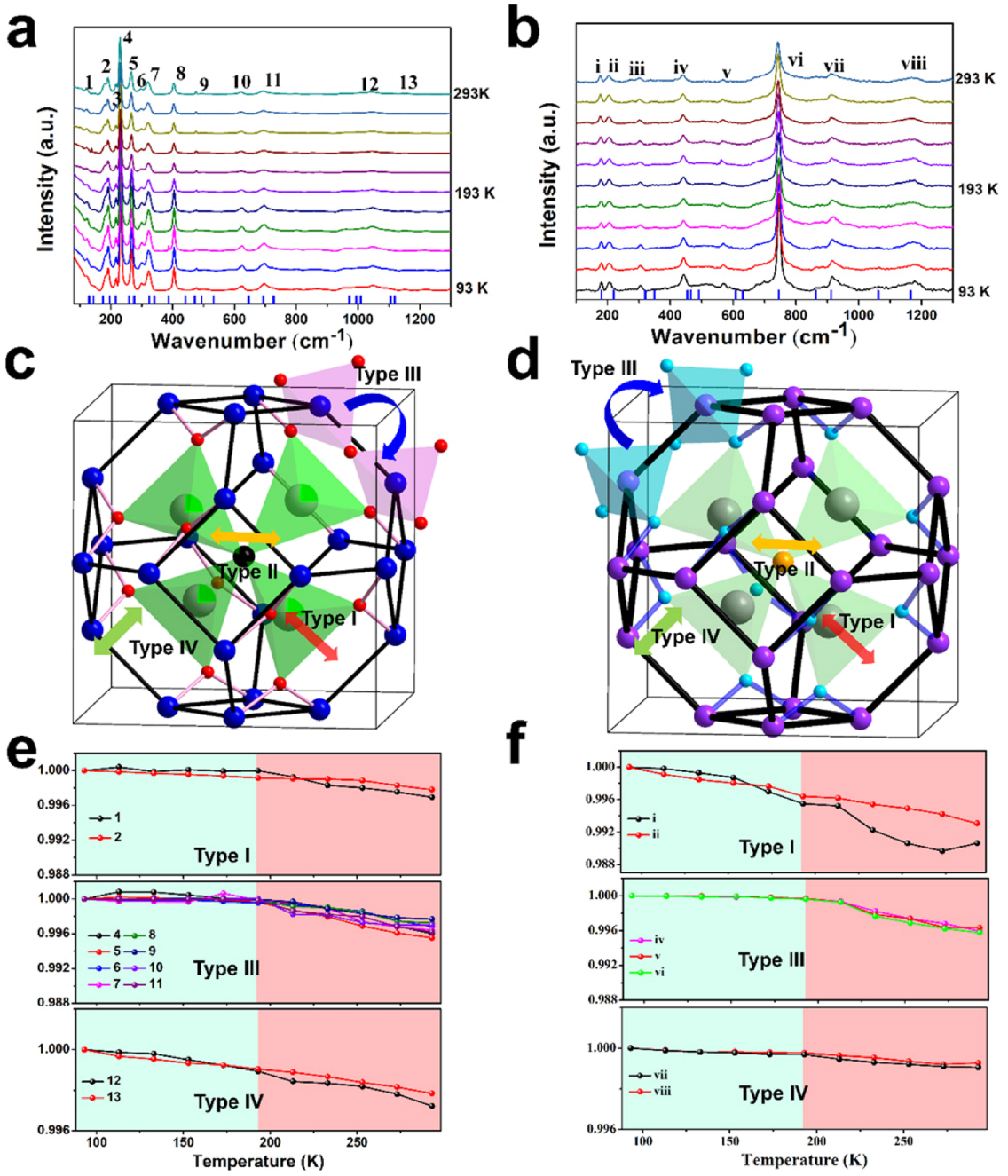

Figure 4. VT-RS in ZGBA (a) and ZPNS (b). The first-principles peak positions are labeled by the blue bars above horizontal axes. Schematic of four types of atomic vibrations by assigning the Raman phonons in ZGBA (c) and ZPNS (d). Frequency variations vs temperature for Type I, Type III, and Type IV phonon modes in ZGBA (e) and ZPNS (f).

rotations of the tetrahedra on sodalite cages. Thus, the corresponding phonon modes are first focused on the lattice dynamical mechanism elaboration of ZTE in ZGBA and ZPNS. As shown in Figure 4e,f (as well as Tables S4−S6), for both compounds, the Raman mode frequencies in Type III vibrations (modes 4−11 in ZGBA and modes iv−vi in ZPNS) almost remain constant from 93 to 193 K, with the largest fluctuation of 0.04%, which coincide with the temperature range of their strict ZTE behaviors below 200 K (with the CTEs of 0.22(24) and 0.58(14) MK^{-1} for ZGBA and ZPNS, respectively; see Figure 3a). As a comparison (see Tables S4−S6), the Raman modes in Type III vibrations in ZBX, taking ZBS as an example, show more prominent red-shifting with the largest fluctuation of 0.17% from 93 to 193 K, consistent with the larger CTEs of 0.69 MK^{-1} below 200 K. This strongly suggests that the extremely low thermal expansions below 200 K in both ZGBA and ZPNS are directly attributed to the hardening of the modes in Type III vibrations. In other words, the $[BO_4]/[PN_4]$ rotation in both compounds is indeed inhibited so as to lead to the lower thermal expansion, compared with ZBX.

To intuitively display the weakened $[BO_4]/[PN_4]$ rotation on sodalite cages in ZGBA and ZPNS, the first-principles simulations on atomic positions with respect to temperature were performed. As shown in Figure 3b and Table S3, as temperature increases from 20 to 300 K, the ∠B−O−B angles

https://doi.org/10.1021/acs.chemmater.2c01947
Chem. Mater. 2022, 34, 9915−9922

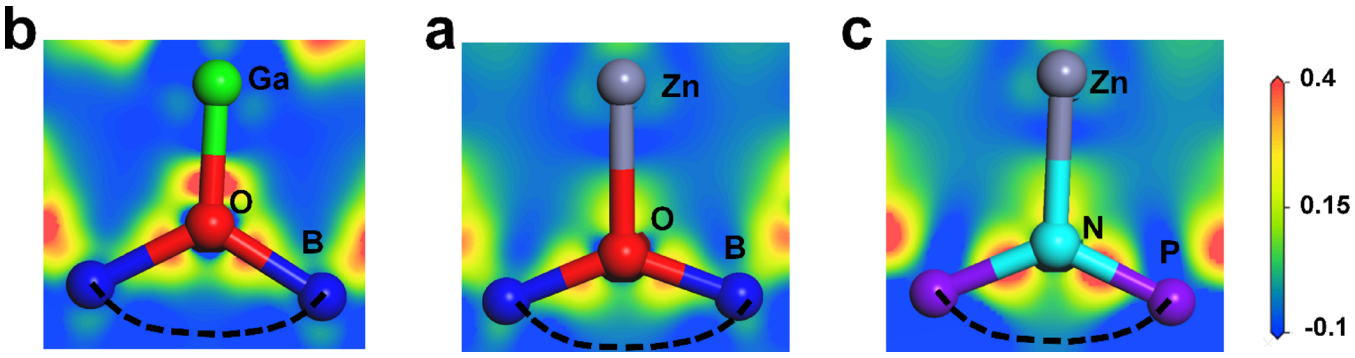

Figure 5. Electron density difference maps on the segments of sodalite cages and the connected Zn/Ga atoms in (a) ZGBA, (b) ZPNS, and (c) ZBS. The segments of sodalite cages are indicated by dashed black curves.

between $[BO_4]$ tetrahedra in ZGBA and ∠P−N−P angles between $[PN_4]$ tetrahedra in ZPNS are only increased from 132.822° to 132.840° (by 0.014%) and from 128.112° to 128.139° (by 0.021%), respectively. These values are much smaller than that in ZBS (from 131.610° to 131.651° by 0.031% for the ∠B−O−B angle), confirming that the smaller rotation of the tetrahedra on sodalite cages with respect to temperature explicitly makes the thermal expansion reduction in the β-sodalite family.

We also investigated the influence of the other three types of atomic vibrations on the thermal expansion behaviors in ZGBA and ZPNS. Type II vibrations account for the vibrations of cage-centered As or S atoms and hardly contribute to the macroscopic thermal expansion.[21] For the Type-I vibrations, the corresponding Raman modes in ZGBA manifest a much weaker phonon softening (by 0.31 and 0.22% for modes 1 and 2, respectively; see Figure 4e and Table S4) than that in ZBS (by 0.62 and 0.45% for modes i and ii, respectively; see Table S6) from 93 to 293 K, while the cousins in ZPNS exhibit a comparable red-shifting (by 0.94 and 0.69% for modes i and ii, respectively; see Figure 4f and Table S5) compared with those in ZBS. As the Type I vibrations characterize the stretching vibrations of the chemical bonds binding to sodalite cages (i.e., $Zn_{0.75}/Ga_{0.25}$−O bonds in ZGBA, Zn−N bonds in ZPNS, and Zn−O bonds in ZBS), the smaller red-shifting of these Raman modes means that the restriction on sodalite cages in ZGBA is strengthened compared to those in ZPNS and ZBS. On the other hand, for the Type IV vibrations, the corresponding Raman modes, modes 12 and 13, in ZGBA are red-shifted by 0.28% and 0.22% from 93 to 293 K, respectively (see Figure 4e and Table S4), which are almost of the same magnitudes of those in ZBS (by 0.08 and 0.17% for modes ix and x, respectively; Table S6), while the red shift of the counterparts in ZPNS (by 0.09 and 0.07% for modes vii and viii, respectively; see Figure 4f and Table S5) is prominently reduced compared with ZBS. As the Type IV vibrations characterize the stretching vibrations of the chemical bonds on sodalite cages, the reduction of the Raman mode shift indicates that the $[P_{24}N_{48}]$ cages are more rigid than the $[B_{24}O_{48}]$ cages in ZBGA and ZBS. Therefore, following the above analysis on all types of atomic vibrations, one may conclude that the enhanced ZTE behaviors in ZGBA and ZPNS are due to the weakened rotations between the $[BO_4]/[PN_4]$ tetrahedra on sodalite cages, which are ascribed to the strengthened restriction forces by Ga/Zn doping in the former compound and the enhanced rigidity of $[P_{24}N_{48}]$ cages in the latter compound.

It is known that the degree of structure modification with respect to temperature in a compound is largely governed by the characteristics of chemical bonds. In order to understand this in ZGBA and ZPNS, their first-principles electron density difference maps[41] are plotted in Figure 5a,b, in comparison with that in ZBS (Figure 5c). Clearly, the charge densities are much more accumulated on the $Zn_{0.75}Ga_{0.25}$−O bonds in ZGBA than on the Zn−O bonds in ZBS, with almost the same charge densities around the B−O bonds between these two compounds. In contrast, the charge densities are much more accumulated on the P−N bonds in ZPNS than on the B−O bonds in ZBS (and in ZGBA), while the charges on the Zn−N bonds are almost the same as those on the Zn−O bonds in ZBS. As a charge density increase indicates the strengthening of chemical bonds, these observations confirm that the $Zn_{0.75}Ga_{0.25}$−O bonds are stronger than the Zn−O bonds and the P−N bonds are stronger (or more rigid) than the B−O bonds, which demonstrate the validity of both structure-regulating approaches, that is, strengthening the binding force to the cage and increasing the rigidity of the sodalite cage, to lower the thermal expansion in the β-sodalite family.

CONCLUSIONS

Summarily, aiming at the ZTE enhancement of isotropic ZTE materials, we proposed two efficient structure-regulating strategies to lower the thermal expansion in the β-sodalite structures: by enhancing the binding force on the cages and by increasing the rigidity of the cage frameworks on the basis of the "cage-restricting" model. Accordingly, taking ZBX template as the parent template, two isotropic ZTE materials, ZGBA and ZPNS, were rationally designed and synthesized via Zn/Ga doping and $[BO_4]/[PN_4]$ replacement, respectively, The CTEs in ZGBA and ZPNS are measured to be 1.18(17)/MK and 1.37(17)/MK, respectively, between 20 and 300 K, both of which are reduced by ∼30−20% compared with the parent templates (ZBX ∼ 1.7/MK). The analysis from lattice dynamics, combined with that from structural evolution and charge difference maps, unravel that the enhanced ZTE behaviors in ZGBA and ZPNS resulted from the weakened rotations of the $[BO_4]/[PN_4]$ tetrahedra on the sodalite cages, which originate from the strengthened restriction on the cages in the former and from the increased rigidity of the cages in the latter compound. Benefited from the enhanced ZTE behaviors, ZGBA and ZPNS are promising materials to be used in the high-precision apparatuses operated in temperature-fluctuating environments. More importantly, the study presented here demonstrates the success of our proposed structure-regulating

https://doi.org/10.1021/acs.chemmater.2c01947
Chem. Mater. 2022, 34, 9915−9922

strategies to the achievement of ZTE materials, which we believe, to open a new avenue to the exploration of ZTE materials in cage-like compounds or even densified framework systems.

■ ASSOCIATED CONTENT

Supporting Information

The Supporting Information is available free of charge at https://pubs.acs.org/doi/10.1021/acs.chemmater.2c01947.

Crystallographic data of ZGBA and ZPNS (ZIP)

Synthesis of ZGBA and ZPNS; crystal structure from 20 to 300 K of ZGBA and ZPNS,; cell parameters; experimental and calculated Raman spectra; temperature-dependent XRD; and temperature-dependent Raman spectrum (PDF)

■ AUTHOR INFORMATION

Corresponding Authors

Xingxing Jiang − *Functional Crystals Lab, Technical Institute of Physics and Chemistry, Chinese Academy of Sciences, Beijing 100190, P.R. China; Center of Materials Science and Optoelectronics Engineering, University of Chinese Academy of Sciences, Beijing 100049, P.R. China*; Email: xxjiang@mail.ipc.ac.cn

Zheshuai Lin − *Functional Crystals Lab, Technical Institute of Physics and Chemistry, Chinese Academy of Sciences, Beijing 100190, P.R. China; Center of Materials Science and Optoelectronics Engineering, University of Chinese Academy of Sciences, Beijing 100049, P.R. China*; orcid.org/0000-0002-9829-9893; Email: zslin@mail.ipc.ac.cn

Authors

Youquan Liu − *Functional Crystals Lab, Technical Institute of Physics and Chemistry, Chinese Academy of Sciences, Beijing 100190, P.R. China; Center of Materials Science and Optoelectronics Engineering, University of Chinese Academy of Sciences, Beijing 100049, P.R. China*; orcid.org/0000-0001-7979-1463

Maxim S. Molokeev − *Laboratory of Crystal Physics, Kirensky Institute of Physics Federal Research Center KSC SB RAS, Krasnoyarsk 660036, Russia; Department of Physics, Far Eastern State Transport University, Khabarovsk 680021, Russia; Siberian Federal University, Krasnoyarsk 660041, Russia*; orcid.org/0000-0002-8297-0945

Xingyu Zhang − *Functional Crystals Lab, Technical Institute of Physics and Chemistry, Chinese Academy of Sciences, Beijing 100190, P.R. China; Center of Materials Science and Optoelectronics Engineering, University of Chinese Academy of Sciences, Beijing 100049, P.R. China*; orcid.org/0000-0003-3753-7779

Complete contact information is available at: https://pubs.acs.org/10.1021/acs.chemmater.2c01947

Notes

The authors declare no competing financial interest.

■ ACKNOWLEDGMENTS

This work was supported by the National Scientific Foundation of China (grant nos 12274425, 51872297, 11974360, and 51890864) and Fujian Institute of Innovation (FJCXY18010201) in CAS. X.X.J. acknowledges the support from Youth Talent Promotion Project from China Association for Science and Technology and the CAS Project for Young Scientists in Basic Research (grant YSBR-024).

■ REFERENCES

(1) Chen, J.; Hu, L.; Deng, J. X.; Xing, X. R. Negative Thermal Expansion in Functional Materials: Controllable Thermal Expansion by Chemical Modifications. *Chem. Soc. Rev.* **2015**, *44*, 3522−3567.

(2) Zhang, Y.; Chen, B.; Guan, D.; Xu, M.; Ran, R.; Ni, M.; Zhou, W.; O'Hayre, R.; Shao, Z. Thermal-Expansion Offset for High-Performance Fuel Cell Cathodes. *Nature* **2021**, *591*, 246−251.

(3) Song, Y. J.; Xu, Y. Z.; Meng, S.; Jiang, X. X.; Shao, C. F.; Song, Z. X.; Zong, N.; Wang, Z. M.; Bo, Y.; Wang, X. J.; Lin, Z. S.; Peng, Q. J. Excellent Performance of a Cryogenic Nd:$YAlO_3$ Laser With Low Wavefront Distortion Based on Zero Thermal Expansion. *Opt. Lett.* **2021**, *46*, 2425−2428.

(4) Wang, W.; Yang, H.; Fu, M. Q.; Zhang, X. Y.; Guan, M. Y.; Wei, Y.; Lin, C. C.; Li, G. G. Superior Thermally-Stable Narrow-Band Green Emitter from Mn^{2+}-Doped Zero Thermal Expansion (ZTE) Material. *Chem. Eng. J.* **2021**, *415*, No. 128979.

(5) Salvador, J. R.; Gu, F.; Hogan, T.; Kanatzidis, M. G. Zero Thermal Expansion in YbGaGe Due to an Electronic Valence Transition. *Nature* **2003**, *425*, 702−705.

(6) Song, Y. Z.; Chen, J.; Liu, X. Z.; Wang, C. W.; Zhang, J.; Liu, H.; Zhu, H.; Hu, L.; Lin, K.; Zhang, S. T.; Xing, X. R. Zero Thermal Expansion in Magnetic and Metallic $Tb(Co,Fe)_2$ Intermetallic Compounds. *J. Am. Chem. Soc.* **2018**, *140*, 602−605.

(7) Ren, Z.; Zhao, R.; Chen, X.; Li, M.; Li, X.; Tian, H.; Zhang, Z.; Han, G. Mesopores Induced Zero Thermal Expansion in Single-Crystal Ferroelectrics. *Nat. Commun.* **2018**, *9*, 1638.

(8) Liu, J.; Maynard-Casely, H. E.; Brand, H. E. A.; Sharma, N. $Sc_{1.5}Al_{0.5}W_3O_{12}$ Exhibits Zero Thermal Expansion between 4 and 1400 K. *Chem. Mater.* **2021**, *33*, 3823−3831.

(9) Hu, L.; Chen, J.; Fan, L. L.; Ren, Y.; Rong, Y. C.; Pan, Z.; Deng, J. X.; Yu, R. B.; Xing, X. R. Zero Thermal Expansion and Ferromagnetism in Cubic $Sc_{1-x}M_xF_3$ (M = Ga, Fe) over a Wide Temperature Range. *J. Am. Chem. Soc.* **2014**, *136*, 13566−13569.

(10) Chen, J.; Xing, X. R.; Sun, C.; Hu, P. G.; Yu, R. B.; Wang, X. W.; Li, L. H. Zero Thermal Expansion in $PbTiO_3$-Based Perovskites. *J. Am. Chem. Soc.* **2008**, *130*, 1144.

(11) Xu, J. L.; Hu, L.; Song, Y. Z.; Han, F.; Qiao, Y. Q.; Deng, J. X.; Chen, J.; Xing, X. R. Zero thermal expansion in cubic $MgZrF_6$. *J. Am. Ceram. Soc.* **2017**, *100*, 5385−5388.

(12) Jiang, X. X.; Molokeev, M. S.; Gong, P. F.; Yang, Y.; Wang, W.; Wang, S. H.; Wu, S. F.; Wang, Y. X.; Huang, R. J.; Li, L. F.; Wu, Y. C.; Xing, X. R.; Lin, Z. S. Near-Zero Thermal Expansion and High Ultraviolet Transparency in a Borate Crystal of $Zn_4B_6O_{13}$. *Adv. Mater.* **2016**, *28*, 7936−7940.

(13) Tao, J. Z.; Sleight, A. W. Very low thermal expansion in TaO_2F. *J. Solid State Chem.* **2003**, *173*, 45−48.

(14) Tallentire, S. E.; Child, F.; Fall, I.; Vella-Zarb, L.; Evans, I. R.; Tucker, M. G.; Keen, D. A.; Wilson, C.; Evans, J. S. O. Systematic and Controllable Negative, Zero, and Positive Thermal Expansion in Cubic $Zr_{1-x}Sn_xMo_2O_8$. *J. Am. Chem. Soc.* **2013**, *135*, 12849−12856.

(15) Ticknor, J. O.; Hester, B. R.; Adkins, J. W.; Xu, W.; Yakovenko, A. A.; Wilkinson, A. P. Zero Thermal Expansion and Abrupt Amorphization on Compression in Anion Excess ReO_3-Type Cubic $YbZrF_7$. *Chem. Mater.* **2018**, *30*, 3071−3077.

(16) Li, S. P.; Huang, R. J.; Zhao, Y. Q.; Wang, W.; Han, Y. M.; Li, L. F. Zero Thermal Expansion Achieved by an Electrolytic Hydriding Method in $La(Fe,Si)_{13}$ Compounds. *Adv. Funct. Mater.* **2017**, *27*, No. 1604195.

(17) Phillips, A. E.; Halder, G. J.; Chapman, K. W.; Goodwin, A. L.; Kepert, C. J. Zero Thermal Expansion in a Flexible, Stable Framework: Tetramethylammonium Copper(I) Zinc(II) Cyanide. *J. Am. Chem. Soc.* **2010**, *132*, 10−11.

(18) Ding, P.; Liang, E. J.; Jia, Y.; Du, Z. Y. Electronic Structure, Bonding and Phonon Modes in the Negative Thermal Expansion Materials of $Cd(CN)_2$ and $Zn(CN)_2$. *J. Phys.: Condens. Mater.* **2008**, *20*, No. 275224.

(19) Song, X.; Sun, Z.; Huang, Q.; Rettenmayr, M.; Liu, X.; Seyring, M.; Li, G.; Rao, G.; Yin, F. Adjustable Zero Thermal Expansion in Antiperovskite Manganese Nitride. *Adv. Mater.* **2011**, *23*, 4690−4694.
(20) Margadonna, S.; Prassides, K.; Fitch, A. N. Zero Thermal Expansion in a Prussian Blue Analogue. *J. Am. Chem. Soc.* **2004**, *126*, 15390−15391.
(21) Morelock, C. R.; Greve, B. K.; Cetinkol, M.; Chapman, K. W.; Chupas, P. J.; Wilkinson, A. P. Role of Anion Site Disorder in the Near Zero Thermal Expansion of Tantalum Oxyfluoride. *Chem. Mater.* **2013**, *25*, 1900−1904.
(22) Cheng, X.; Yuan, J.; Zhu, X.; Yang, K.; Liu, M.; Qi, Z. Origin of Negative Thermal Expansion in Zn_2GeO_4 Revealed by High Pressure Study. *J. Phys. D: Appl. Phys.* **2018**, *51*, No. 095303.
(23) Hu, L.; Chen, J.; Xu, J. L.; Wang, N.; Han, F.; Ren, Y.; Pan, Z.; Rong, Y. C.; Huang, R. J.; Deng, J. X.; Li, L. F.; Xing, X. R. Atomic Linkage Flexibility Tuned Isotropic Negative, Zero, and Positive Thermal Expansion in $MZrF_6$ (M = Ca, Mn, Fe, Co, Ni, and Zn). *J. Am. Chem. Soc.* **2016**, *138*, 14530−14533.
(24) Evans, J. S. O.; Mary, T. A.; Vogt, T.; Subramanian, M. A.; Sleight, A. W. Negative Thermal Expansion in ZrW_2O_8 and HfW_2O_8. *Chem. Mater.* **1996**, *8*, 2809−2823.
(25) Liu, Y.; Mei, D.; Wang, N.; Molokeev, M. S.; Jiang, X.; Lin, Z. Intrinsic Isotropic Near-Zero Thermal Expansion in $Zn_4B_6O_{12}X$ (X = O, S, Se). *ACS Appl. Mater. Interfaces* **2020**, *12*, 38435−38440.
(26) *Bruker AXS; TOPAS V4: General Profile and Structure Analysis Software for Powder Diffraction Data*; User's Manual; Bruker AXS: Karlsruhe, Germany, 2008.
(27) Burgess, S.; Sagar, J.; Holland, J.; Li, X.; Bauer, F. Ultra-Low kV EDS − A New Approach to Improved Spatial Resolution, Surface Sensitivity, and Light Element Compositional Imaging and Analysis in the SEM. *Microsc. Today* **2017**, *25*, 20−29.
(28) Cliffe, M. J. G. PASCal: a Principal Axis Strain Calculator for Thermal Expansion aAnd Compressibility Determination. *J. Appl. Crystallogr.* **2012**, *45*, 1321−1329.
(29) Clark, S. J.; Segall, M. D.; Pickard, C. J.; Hasnip, P. J.; Probert, M. J.; Refson, K.; Payne, M. C. First Principles Methods Using CASTEP. *Z. Kristallogr.* **2005**, *220*, 567−570.
(30) Payne, M. C.; Allan, D. C.; Arias, T. A.; Joannopoulos, J. D. CASTEP 4.2 Academic Version, Licensed under the UKCP-MSI Agreement. *Rev. Mod. Phys.* **1992**, *64*, 1045.
(31) Perdew, J. P.; Burke, K.; Ernzerhof, M. Generalized gradient approximation made simple. *Phys. Rev. Lett.* **1996**, *77*, 3865−3868.
(32) Perdew, J. P.; Wang, Y. Pair-Distribution Function and its Coupling-Constant Average for the Spin-Polarized Electron-Gas. *Phys. Rev. B: Condens. Matter Mater. Phys.* **1992**, *46*, 12947−12954.
(33) Hamann, D. R.; Schluter, M.; Chiang, C. Norm-Conserving Pseudopotentials. *Phys. Rev. Lett.* **1979**, *43*, 1494−1497.
(34) Monkhorst, H. J.; Pack, J. D. Special Points for Brillouin-Zone Integrations. *Phys. Rev. B: Solid State* **1976**, *13*, 5188−5192.
(35) Pfrommer, B. G.; Côté, M.; Louie, S. G.; Cohen, M. L. Relaxation of Crystals with the Quasi-Newton Method. *J. Comput. Phys.* **1997**, *131*, 233−240.
(36) Baroni, S.; de Gironcoli, S.; Dal Corso, A.; Giannozzi, P. Phonons and Related Crystal Properties from Density-Functional Perturbation Theory. *Rev. Mod. Phys.* **2001**, *73*, 515−562.
(37) Cochran, W.; Fray, S. J.; Johnson, F. A.; Quarrington, J. E.; Williams, N. Lattic Absorption in Gallium Arsenide. *J. Appl. Phys.* **1961**, *32*, 2102−2106.
(38) Hu, P. H.; Chen, J.; Deng, J. X.; Xing, X. R. Thermal Expansion, Ferroelectric and Magnetic Properties in $(1\text{-}x)PbTiO_3$-$xBi(Ni_{1/2}Ti_{1/2})O_3$. *J. Am. Chem. Soc.* **2010**, *132*, 1925−1928.
(39) Bridges, F.; Keiber, T.; Juhas, P.; Billinge, S. J. L.; Sutton, L.; Wilde, J.; Kowach, G. R. Local Vibrations and Negative Thermal Expansion in ZrW_2O_8. *Phys. Rev. Lett.* **2014**, *112*, No. 045505.
(40) Gava, V.; Perotton, C. A. First-Principles Mode Gruneisen Parameters and Negative Thermal Expansion in α-ZrW_2O_8. *Phys. Rev. Lett.* **2012**, *109*, No. 195503.
(41) Belpassi, L.; Infante, I.; Tarantelli, F.; Visscher, L. The chemical bond between Au(I) and the noble gases. Comparative study of NgAuF and $NgAu^+$ (Ng = Ar, Kr, Xe) by density functional and coupled cluster methods. *J. Am. Chem. Soc.* **2008**, *130*, 1048−1060.

https://doi.org/10.1021/acs.chemmater.2c01947
Chem. Mater. 2022, 34, 9915−9922